applied sciences

MDPI

Article

Digital Rock Analysis on the Influence of Coarse Micro-Fractures on Petrophysical Properties in Tight Sandstone Reservoirs

Lei Liu [1,2], Jun Yao [1,2,*], Hai Sun [1,2], Lei Zhang [1,2] and Kai Zhang [1,2]

[1] School of Petroleum Engineering, China University of Petroleum (East China), Qingdao 266580, China
[2] Research Centre of Multi-Phase Flow in Porous Media, China University of Petroleum (East China), Qingdao 266580, China
* Correspondence: rcogfr_upc@126.com

Abstract: Tight sandstone reservoirs, as typical unconventional reservoirs, have attracted more and more attention worldwide. Compared to conventional reservoirs, the complex microscopic pore structures and micro-fractures of the tight reservoirs are developed, and fluid flow in the tight sandstone reservoir is very complicated. Therefore, studying the influence of fractures on the rock topological structure and the flow characteristics between micro-fractures and the matrix is critical to the development of tight sandstone reservoirs. In light of the intricate nature of micro-fractures, digital rock analysis technology is utilized to address this issue instead of traditional experimental methods. Firstly, the selected tight rock is scanned by X-ray computed tomography (XCT), and then the natural tight digital rock is reconstructed by filtering and binary segmentation. Secondly, micro-fracture with different shapes is added to the digital rock. Then, a pore network model extracted by the maximum ball method is adopted to conduct the flow simulation. The study finds that the distribution of pore throat radius changes with increasing fracture aperture and length and that the permeability and capillary pressure curves are influenced by fracture aperture and length in the direction of connectivity. The impact of micro-fracture dip angle on pore throat structure is significant with changes in permeability and fluid flow in different directions. Overall, the study emphasizes the importance of fracture aperture and length in determining the properties and behavior of tight sandstone reservoirs and highlights the usefulness of digital rock analysis technology in providing insights into complex microstructures.

Keywords: tight sandstones reservoirs; micro-fracture; pore scale modeling; digital rock; roughness

check for updates

Citation: Liu, L.; Yao, J.; Sun, H.; Zhang, L.; Zhang, K. Digital Rock Analysis on the Influence of Coarse Micro-Fractures on Petrophysical Properties in Tight Sandstone Reservoirs. *Appl. Sci.* **2023**, *13*, 5237. https://doi.org/10.3390/app13095237

Academic Editor: Giuseppe Lacidogna

Received: 17 February 2023
Revised: 6 April 2023
Accepted: 20 April 2023
Published: 22 April 2023

Copyright: © 2023 by the authors. Licensee MDPI, Basel, Switzerland. This article is an open access article distributed under the terms and conditions of the Creative Commons Attribution (CC BY) license (https://creativecommons.org/licenses/by/4.0/).

1. Introduction

In recent years, unconventional reservoirs, such as tight sandstone oil and gas, have become increasingly popular in the petroleum industry due to their wide distribution and abundance of subsurface reserves [1–4]. Tight sandstone reservoirs contain oil and gas with low connectivity between pores, ranging in size from nano-scale to micro-scale, resulting in low porosity and permeability [5,6]. Horizontal drilling and hydraulic fracturing technology have become essential due to the complexity of the naturally formed micro-fractures and the artificial fractures created by stimulating the reservoir volume [7]. These fractures significantly impact the fluid flow patterns and the capacity of extraction [8]. For this reason, geologists and engineers must study the micro-fracture's effect on petrophysical properties [9].

The presence of micro-fractures can enhance the porosity and permeability of rock by altering the connection of tight sandstone reservoirs. However, whether micro-fractures cause pore structure changes in tight sandstone reservoirs is unclear. The petrophysical properties include permeability, capillary pressure, and relative permeability which are functions of pore structure [10] and are the most important parameters to describe fluid flow within micro-fractures. Furthermore, it is common to apply the cubic law to describe

fluid flow within micro-fractures which are viewed as parallel plates with impermeable and smooth walls [11]. On the other hand, the oil and gas flow between micro-fractures and matrix pores are not considered [12]. In reality, due to filling with mineral cement or proppant, complicated micro-fractures tend to be coarse and curved [13]. Hence, to accurately describe the oil and gas flow within micro-fractures, the impact of surface roughness, aperture distribution, length, and matrix-fractures transfer must be accounted for.

Recently, many researchers have conducted experiments [13] and developed numerical models [14,15] to investigate the oil and gas flow in micro-fractures at the pore scale which was initially simplified by reducing the parallel plates to single fractures and deriving the well-known cubic law. However, experiments have revealed the micro-fractures' complexity, ranging from the distribution of aperture and roughness to length and inclination. This stresses the significance of quantifying the roughness in order to accurately capture the effect of the fractures' structure on the capacity to transport fluids. Several experiments have been conducted to explore the fluid flow in rough-walled micro-fractures which have reported favored flow channels and convoluted pathways [16]. The majority of such studies use single flows and artificial samples, though pore-scale experimental measurements are often challenging, costly, and time-consuming.

Beyond experiment technology, a numerical model can also provide a tool to measure and describe the oil and gas flow in micro-fracture with the microstructure of fracture. More recently, with the development of visualization and computer techniques, pore-scale modeling, as a recent approach, has been used to investigate the petrophysical properties of porous media. According to the numerical approaches used to simulate oil and gas flow processes, these can be divided into two classes: pore-scale modeling with image-based data and pore network modeling [17,18]. Pore-scale modeling with image-based methods includes particle-based methods, such as the lattice Boltzmann method (LBM) [19,20], and mesh-based approaches, such as finite difference [21], finite volume [22], and finite element method [23]. Additionally, for multi-phase flow, the level set [24], phase field [25], and smoothed-particle hydrodynamic (SPH) methods [26] can be used to define an interface between fluids and track their movement. On the other hand, pore network modeling [27] involves extracting an idealized and representative pore network from the image, followed by the computation of relevant petrophysical properties and oil and gas flow simulations.

With pore-scale modeling and an image-based approach, the processes of reactive transport [28], multi-phase fluid flow [29], and heat transfer [30] were simulated in micro-fractures. However, the micro-fracture model assumptions are too simple. Other researchers used the pore network modeling method to investigate multi-phase fluid flow in horizontal, rough-walled micro-fractures [31]. They disregarded the effects of gravity and viscous forces and also believed that the impact of local fracture wall convergence or divergence could be disregarded. They looked at the combined impact of the two main curvature radii, in plane and aperture induced. Pore-scale imaging and modeling have also been used to explore how contact angles and void structures affect capillary pressure and relative permeability properties. However, there were some shortcomings: (1) The effect of rough-walled micro-fractures on single- and multi-phase flow is not evaluated. (2) The description of micro-fractures roughness in current models is not accurate. (3) The transmission relation between the matrix and the micro-fracture should be considered in the process of heat and mass simulation. Actually, the petrophysical properties are the function of the pore structure of the matrix and micro-fractures.

In fact, the real micro-fractures have variable apertures, lengths, and inclinations which create roughness for fluid to flow [32–34]. It is discovered that non-Euclidian fractal geometry with a self-affine law may adequately explain the intricate geometry of micro-fractures surface. The fractal dimension is a useful parameter to describe the real surface behavior of micro-fractures.

This paper is organized as follows: First, X-ray computed tomography (XCT) imaging technology was used to scan the rock sample from tight sandstone reservoirs. The representative elementary volume of digital rock was obtained using image processing, including

filtering and segmentation. Secondly, the method was introduced to generate a rough surface. The related parameters were determined to reconstruct rough-walled micro-fractures for the next simulation. Thirdly, the approaches to computing pore structure and petrophysical properties were introduced in Section 2. Micro-fracture digital rocks were generated, combining random rough surfaces with the digital rock. In Section 3, the micro-fracture parameters, such as aperture, length, and dip angle, were considered to carry out the effect of the micro-fracture on the pore structure and petrophysical properties. In Section 4, the conclusions were obtained.

2. Materials and Methods

2.1. XCT Imaging and Processing

Due to its non-destructive nature in three-dimension, XCT has evolved into a widely employed technique for visualizing and characterizing geological specimens in three-dimension. The tight rock sample we used in this study was sampled from the Long 7 well of the extension group developed in the center of the Ordos Basin Lake Basin in China which is generally composed of various minerals (such as quartz, feldspar, pyrite, and others) and significant pores and micro-fractures, see Figure 1a. Tomographic datasets, which are series of images based on gray-scale value, were obtained and analyzed using an X-ray Micro-CT-400 made by the Xradia Company. The resolution is 1.0 μm/voxel, and the voxel size is 1024 × 1024 × 1024. Some scholars had begun to explore multi-phase segmentation considering multi-minerals [35–37]; however, the focus of this study was to investigate the impact of micro-fracture characteristics on petrophysical properties. Therefore, the study applied the two-step method to identify the pore and grain space. A non-local means filtering, a nonlinear filter used to enhance the signal-to-noise ratio and preserve the edges between pore and grain phases in XCT images, was utilized. Subsequently, a marker-seeded watershed algorithm [38] was employed to segment the images into pore and grain phases, as shown in Figure 1b. This method depends on the image's intensity field and intensity gradient magnitudes with the seed markers produced using 2D histograms.

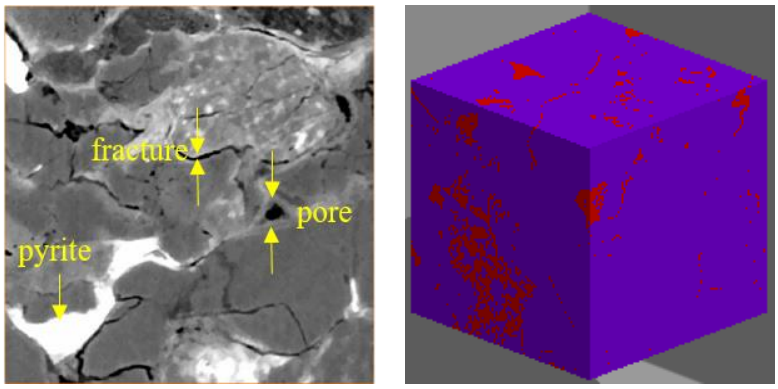

(**a**) Gray-scale image (**b**) Tight digital rock

Figure 1. The sample of tight sandstone. (**a**) is the gray-scale image of the tight sample, (**b**) is the tight digital rock. The red color represents pore space and purple color indicates grain space.

For the convenience of subsequent simulations, a representative elementary volume (REV) should be selected. The REV of the tight samples refers to the smallest unit that can effectively characterize the tight sample's physical properties. The physical properties calculated from the REV of the tight sample are the same as the physical properties of the whole tight sample.

In this paper, the size of the REV of the tight sample is obtained by analyzing the porosity variation with the tight digital rock size. The specific method is as follows: First, locating a voxel point arbitrarily in the tight digital rock; selecting a cube of a certain variable length at the center of the voxel point and counting its porosity and permeability, gradually

increasing the side length of the cube and calculating the porosity and permeability of each side length rock cube; making the variation law curve of porosity and permeability with the side length of tight digital rock (see Figure 2); locating different voxel centers and repeating the above steps. However, the minimum rock edge length corresponding to the stabilization of all the curves is the size of the REV. The core voxel size selected after analysis is 500^3.

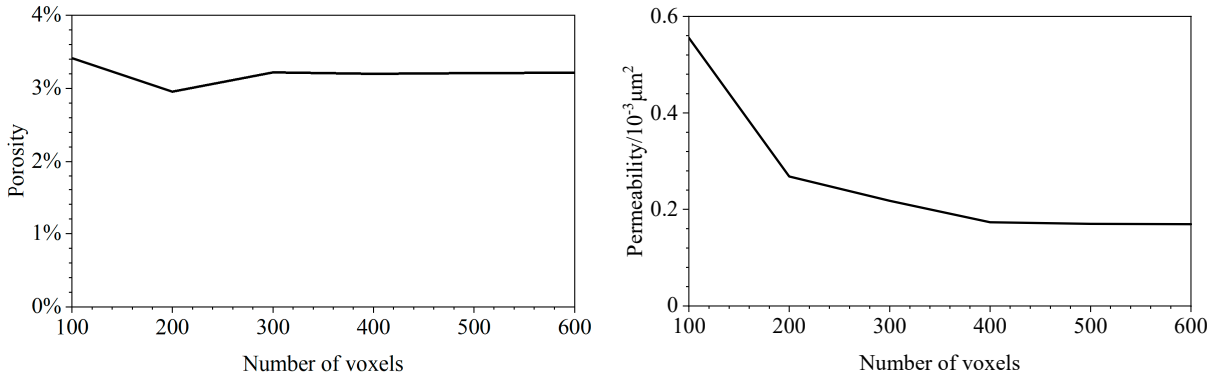

(**a**) Porosity vs. number of voxels (**b**) Permeability vs. number of voxels

Figure 2. The result of REV analysis is based on porosity and permeability. (**a**) is for porosity and (**b**) is for permeability.

2.2. Embedding a Random Surface of Micro-Fracture

Tight sandstone reservoir develops a large number of micro-fractures after hydraulic fracturing. In this paper, the artificial surface roughness is characterized by its spatial frequency content. The random artificial surface can be considered as many elementary waves. A sum of trigonometric functions is employed to construct the random artificial surface, which is analogous to a Fourier series expansion. Each term in the sum represents a specific frequency oscillation in space. The artificial surface can be described as follows.

$$f(x,y) = A_{mn} \times \sum_{m=-M}^{M} \sum_{n=-N}^{N} \sin(\pi(mx + ny) + \phi(m,n)), \tag{1}$$

$$A_{mn} = \sum_{m=-M}^{M} \sum_{n=-N}^{N} \frac{1}{|m^2 + n^2|^{f_D}}. \tag{2}$$

In this equation, $f(x,y)$ represents the artificial random surface data with amplitude. A_{mn}, m and n are the numbers of waves in the X and Y directions, respectively. M and N represent the largest numbers of waves in the X and Y directions, respectively. f_D is the surface fractal dimension, and $\phi(m,n)$ are phase angles. Although the equation is expressed in sinusoidal functions, the inclusion of phase angles allows for a general trigonometric series to be expressed according to the angle sum rule.

To achieve a natural-looking surface, a suitably small portion should be "cut out" by limiting the variation of x and y to specific values as the periodicity of the synthesized data will otherwise be evident given the periodic nature of the function by definition. In three-dimensional space, the micro-fracture has two sides. Two random surfaces need to be constructed with different random phase angles to generate a whole micro-fracture. On the other hand, the relative parameters should be selected to generate a natural-looking micro-fracture. The numbers of waves affect the intensity of the amplitude. To synthesize a surface with no preferred direction of oscillations, we can assign both positive and negative values to m and n with equal probabilities. The surface fractal dimension influences surface roughness.

In order to choose reasonable parameters, different artificial random surfaces are generated in Figures 3 and 4. In Figure 3, the largest number of waves in different directions

is equivalent to 50. In Figure 3a–d, the surface fractal dimensions differ with 0.5, 1.0, 1.5, and 1.8. In Figure 3, the surface fractal dimensions are 1.5, and the largest waves in different directions are equivalent. In Figure 4a–d, the largest numbers of the waves are different with 20, 40, 60, and 80. By comparing Figures 3 and 4, the largest number of the waves in different directions are equivalent to selecting 40. The surface fractal dimensions are determined at 1.6. In the following study, the artificial random micro-fractures are constructed with the largest numbers of waves and the surface fractal dimensions to ensure the micro-fracture's surface is natural looking. The phase angles will be used randomly to generate the random surface.

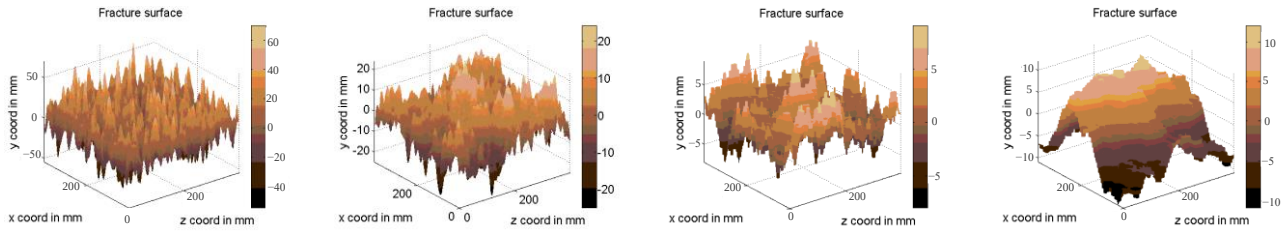

(**a**) f_D = 0.5 (**b**) f_D = 1.0 (**c**) f_D = 1.5 (**d**) f_D = 1.8

Figure 3. The rough-walled surface with different surface fractal dimensions. (**a**) shows the random fracture surface for f_D = 0.5, (**b**) is the random fracture surface for f_D = 1.0, (**c**) represents the random fracture surface for f_D = 1.5, and (**d**) displays the random fracture surface for f_D = 1.8.

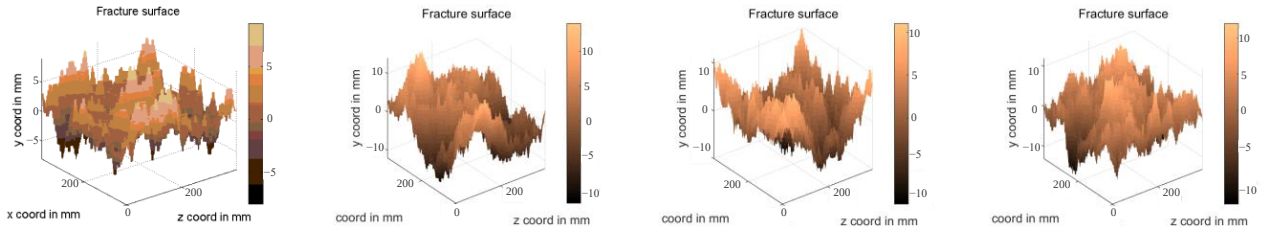

(**a**) M = 20 (**b**) M = 40 (**c**) M = 60 (**d**) M = 80

Figure 4. The rough-walled surface with different numbers of waves. (**a**) shows the random fracture surface for M = 20, (**b**) is the random fracture surface for M = 40, (**c**) represents the random fracture surface for M = 60, and (**d**) displays the random fracture surface for M = 80.

2.3. Pore structure and Petrophysical Properties Analysis

Pore-scale modeling with pore network can quantitatively describe the pore structure and simulate fluid flow. The pore network is a reduced-dimension representation of the pore space and, in its simplest form, consists of an interconnected set of pore nodes and bonds. Pore-scale modeling with pore network is computationally much more efficient than the direct simulation approaches.

2.3.1. Extraction of Pore Network

For pore network models to accurately predict multi-phase displacement mechanisms, it is essential to accurately characterize the pore structure. The process of pore network extraction can be divided into two stages: splitting the pore space representation into discrete elements and measuring the geometric properties of each network element. These properties, such as inscribed radius, length, volume, and shape parameters, are then used in flow modeling. Firstly, the medial axis was obtained to represent the pore space via skeletonization in the context of topology-based analysis [39]. Subsequently, the well-known morphology-based method is the extraction of maximal balls, the largest inscribed spheres that touch the grain or boundary and are centered on each image voxel. The fully contained spheres are then removed. The maximal balls describe the pore space without redundancy and are clustered into families based on their size and overlap with other

maximal balls. The largest maximal balls identify pores, while the smallest, which belong to more than one family and connect the pores identified by these families are throats [40]. Then the pore network was obtained from digital rock. In this study, a pore network was used to characterize pore structure and simulate fluid flow processes due to the presence of micro-fractures.

2.3.2. Porosity, Permeability and Capillary Pressure

To quantitatively characterize the effect of micro-fractures on fluid flow, we have selected porosity, permeability, and capillary pressure as key parameters. Specifically, the porosity is calculated as the percentage of pore pixels in relation to the total number of pixels.

Through the application of mass conservation in each pore throat of the pore network model, we can analyze the single-phase fluid flow in each direction of the network and calculate the permeability using Darcy's law. The boundary condition is a constant pressure boundary condition; only the value of the pressure drop needs to be considered, and the general value can be taken as a reference.

$$K_i = \frac{\mu q_i L}{A(P_{\text{in}} - P_{\text{out}})}, \tag{3}$$

where K_i is the absolute permeability in i direction, μm^2, μ is the viscosity of the fluid, mPa·s; q_i is the total flow at the pressure difference across the model when the model is fully saturated, cm^3/s; L is the length, cm; A is the cross-sectional area, cm^2.

For mercury intrusion, the mercury is injected at a constant rate from the inlet, the whole pressure will be computed. The capillary pressure curves can be obtained in each direction.

3. Results

To study the effect of micro-fractures on the pore structure and petrophysical properties of tight sandstone reservoirs, a single micro-fracture is selected because a single micro-fracture is the most basic unit in the discrete fracture network of tight sandstone reservoirs. In the low-resolution of the rock sample in tight sandstone reservoirs, the fractures were complex. The values of aperture, length, and dip angle were summarized from low-resolution CT images. Based on the acquired digital rock of tight sandstone reservoirs, embedding a single fracture of different aperture, length, and dip and then studying the impact of micro-fracture on the pore structure, permeability, and capillary pressure.

3.1. Embedding an Artificial Micro-Fracture with Different Aperture

Based on the digital rock of the tight sandstone reservoir obtained from XCT technology, the artificial micro-fracture model is added with a dip of 0 degrees and a length of 500 voxels (penetrating), followed by a voxel ranging from 2 voxels to 50 voxels with a resolution of 1.0 μm/voxel to form a multi-scale digital rock as shown in Figure 5. Due to the artificial micro-fracture surface's roughness, some spots have closed micro-fractures while others have larger micro-fracture apertures than desired. However, the average aperture of the micro-fracture is the set value. The micro-fracture is close to the real situation. Figure 4 also shows the pore network model for multi-scale digital rock extraction of tight sandstone reservoirs using the maximal balls method with 0.6 h. The micro-fracture was treated as a series of interconnected pores and throats.

In order to further analyze the effect of micro-fracture on the pore structure for tight sandstone reservoirs, the pore radius, and throat radius distribution were plotted, see Figures 6a and 6b, respectively. In Figure 6, different colors represent different models for where the original model obtained from XCT technology is red, while the green, blue, and pink hues embody models with micro-fracture apertures of 10 μm, 30 μm, and 50 μm, respectively. All curves for pore radius and throat radius distribution have a similar trend. For pore radius distribution, the size of the pore expands as the micro-fracture aperture increases, especially if the micro-fracture aperture is more than 10 μm. For throat radius

distribution, the size of the throat expands as the micro-fracture aperture increases due to the existence of the micro-fracture.

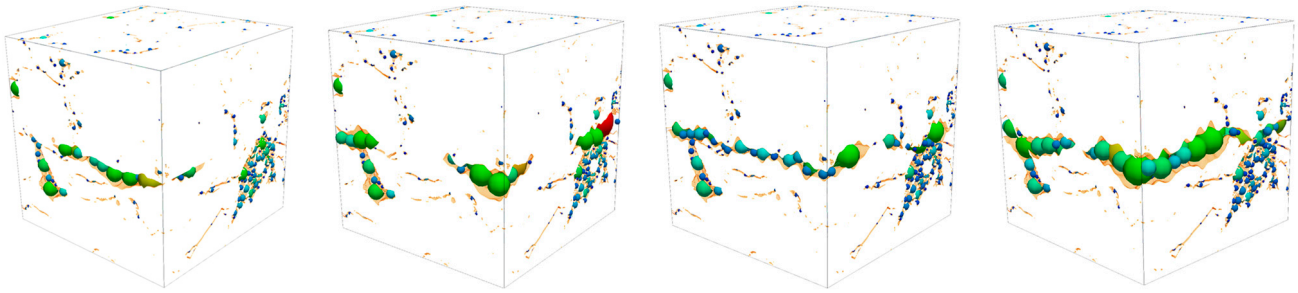

(**a**) aperture = 2 μm (**b**) aperture = 10 μm (**c**) aperture = 30 μm (**d**) aperture = 50 μm

Figure 5. The digital rocks embedding an artificial fracture with a different aperture and pore networks extracted using the maximal balls method. (**a**) shows the digital rock and pore network with the micro-fracture whose aperture is 2 μm, (**b**) is the digital rock and pore network with the micro-fracture whose aperture is 10 μm, (**c**) represents the digital rock and pore network with the micro-fracture whose aperture is 30 μm, and (**d**) displays the digital rock and pore network with the micro-fracture whose aperture is 50 μm.

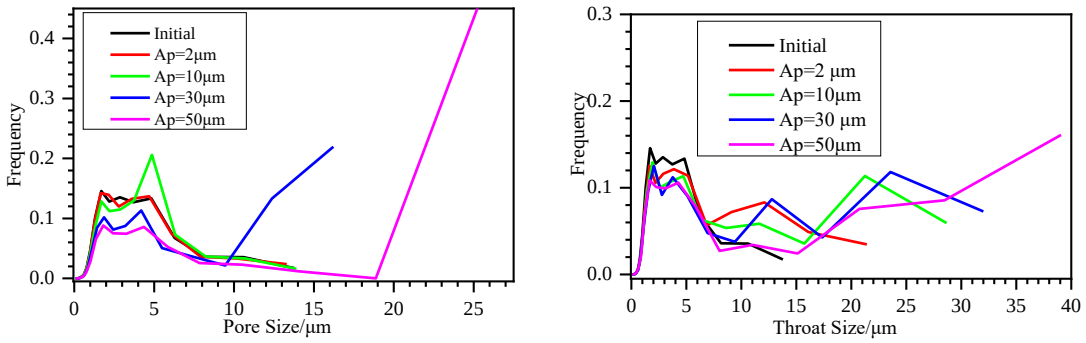

(**a**) Pore radius distribution (**b**) Throat radius distribution

Figure 6. The pore structure distribution of the embedding an artificial fracture with different aperture. (**a**) is the pore radius distribution, and (**b**) is the throat radius distribution.

The presence of the micro-fracture significantly changed the pore structure of tight sandstone reservoirs. Altering the radius of the pores and throats can substantially enhance the fluid flow conditions. This factor also underscores the significance of hydraulic fracturing in enhancing recovery. To further assess the significance of quantitatively evaluating the micro-fracture, the impact of varying pore and throat radii on permeability was computed and graphed. The formula used to calculate the influence of distinct pore and throat radii on permeability is expressed as follows:

$$\Delta K_i = \frac{r_i^2 * \alpha_i}{\sum r_i^2 * \alpha_i}. \tag{4}$$

For the i th interval, the permeability contribution value is denoted by ΔK_i, the corresponding pore or throat radius value is represented by r_i, and its frequency is given by α_i.

The impact of varying pore and throat radii on permeability was plotted in Figure 6a,b. In Figure 7, different colors represent different models. In comparison with the initial digital rock model, the curves of the digital rock with a different aperture for pore and throat are bimodal distributions. In Figure 7a,b, as the micro-fracture aperture increases, a new peak emerges in the curve, indicating that the fracture is beginning to impact the permeability.

Once the micro-fracture aperture exceeds 10 μm, the influence of the micro-fracture on permeability outweighs the impact of the initial model on permeability.

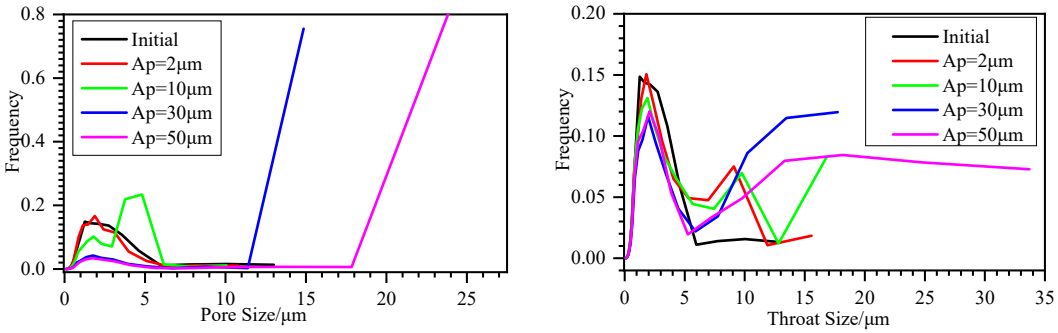

(**a**) The contribution for permeability of the pore (**b**) The contribution for permeability of the throat

Figure 7. The contribution for permeability of embedding an artificial fracture with different apertures. The pore's contribution to permeability is (**a**) while the throat's contribution to permeability is (**b**).

The evaluation of the impact of pore and throat permeability is currently limited to theoretical analysis. One approach to calculating the porosity and permeability of various models involves the utilization of pore network modeling methods. The effect of the micro-fracture aperture on the permeability of the tight sandstone reservoir in different directions is shown in Table 1. The time needed for each pore network model is 0.1 h. The porosity of a rock can increase as micro-fractures within the rock become more open. This is due to the fact that micro-fractures can greatly enhance the connectivity between pores within the rock, allowing fluids to flow more freely, see Figure 5. As the fractures widen, the volume of open space within the digital rock also increases, increasing overall porosity. It is important to note that the relationship between fracture opening and porosity can be complex and depends on various factors. Analyzing the permeability in different directions can provide valuable insights into how micro-fractures affect fluid flow. It is easy to find that with the increase in micro-fracture aperture, the permeability increases significantly in the X and Y directions, and the permeability in the Z direction also increases, but the magnitude is significantly smaller than that in the X and Y directions. As a general trend, when a micro-fracture is parallel to the flow direction, it can significantly increase the permeability in that direction. This is because the micro-fracture provides a clear and unobstructed pathway for fluid flow. On the other hand, when a micro-fracture is perpendicular to the flow direction, the increase in permeability may not be as noticeable. This is because the micro-fracture does not provide as direct a pathway for fluid flow in that direction.

Table 1. The porosity and permeability of the embedding an artificial fracture with different aperture.

Different Aperture	Porosity/%	Permeability/10^{-3} μm^2		
		X Direction	Y Direction	Z Direction
Initial	3.21	0.17	0.01	0.10
Ap = 2 μm	7.99	1.33	2.80	1.67
Ap = 10 μm	8.55	18.33	21.92	2.87
Ap = 30 μm	16.17	2625.91	2968.03	2.98
Ap = 50 μm	23.76	6356.13	7066.84	2.99

To further examine the influence of micro-fracture on fluid flow, capillary pressure curves in different directions which were presented in Figure 8. The data reveals that, compared to the original model, the capillary pressure curves in the X and Y directions shift towards the left as the micro-fracture opening widens. Furthermore, the capillary pressure curves in these directions exhibit significant changes when the micro-fracture opening exceeds 10 μm. However, as observed in the permeability at different directions, the capillary pressure curves in the Z direction display minimal changes. This phenomenon is

attributed to micro-fractures that run parallel to the XY plane. Capillary pressure curves are frequently utilized to assess the pore structure characteristics of rocks and can be beneficial for predicting fluid flow behavior in porous media. By comparing the capillary pressure curves in different directions, it is possible to establish the relationship between the curves and the direction of fluid flow. It is essential to consider the orientation of micro-fractures when analyzing the pore structure of cores that contain such micro-fractures indirectly through capillary force curves.

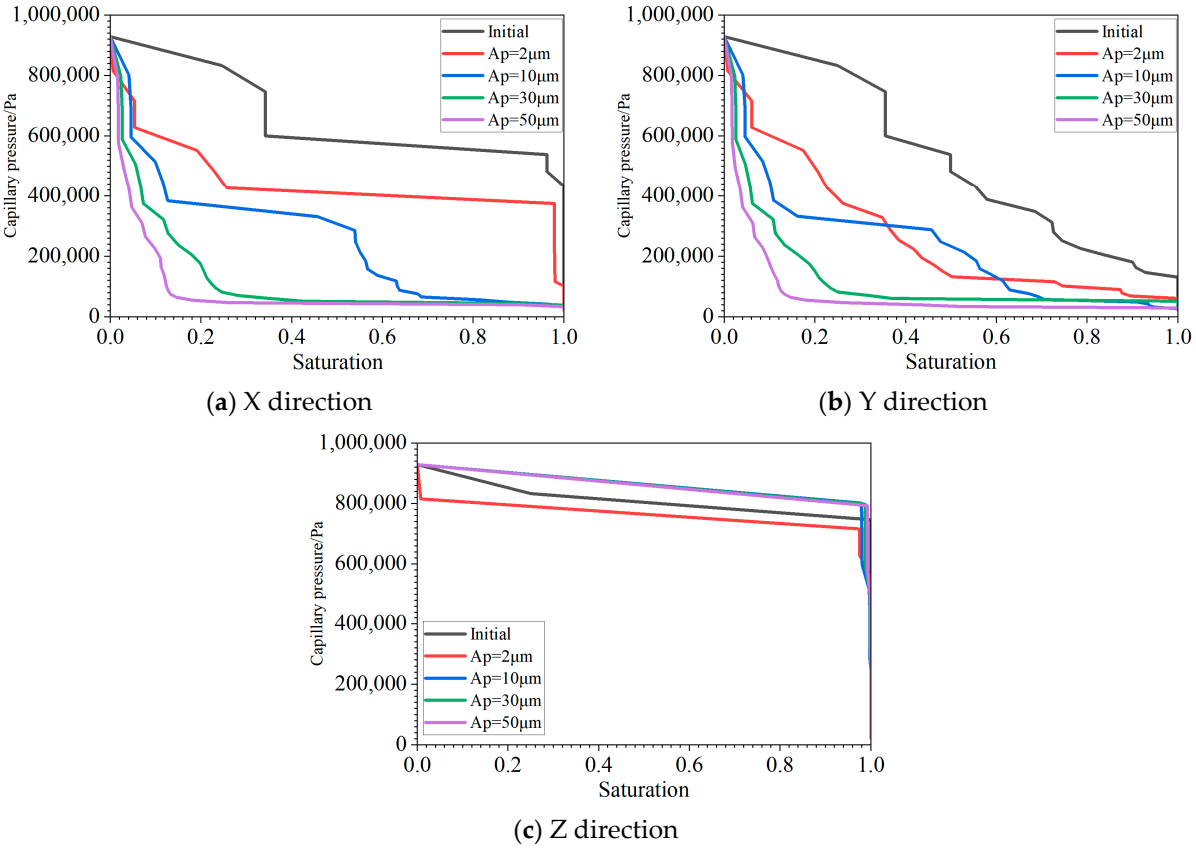

(**a**) X direction (**b**) Y direction

(**c**) Z direction

Figure 8. The capillary pressure curve of embedding an artificial fracture with a different aperture in different directions. (**a**) X direction, (**b**) Y direction, (**c**) Z direction.

3.2. Embedding an Artificial Micro-Fracture with Different Length

To further investigate the impact of micro-fracture length on tight sandstone reservoirs, we incorporated a single fracture into the digital rock of the reservoir with an inclination of 0 degrees and an aperture of 10 voxels. The fracture length varied from 50 to 450 voxels in a sequential manner, resulting in a multi-scale digital rock as illustrated in Figure 9. The pore network model of the resulting tight sandstone reservoir multi-scale digital rock was then extracted using the maximal balls method with 0.6 h, as depicted in Figure 9.

Figure 10 shows the pore structure distribution of the embedding of artificial fracture with different lengths, demonstrating the influence of micro-fracture length on the pore throat structure. As illustrated, the distribution of pore and throat radius shifts from a single-peaked Gaussian distribution to a double-peaked and multi-peaked distribution with increasing fracture length. Notably, this is particularly evident in the distribution of throat radius.

The contribution of pore and throat radius to permeability is depicted in the relationship curves shown in Figure 11. These curves reveal that the range in which pore and throat radius contribute to the larger permeability value is relatively similar to that of the original digital rock. However, the contribution to permeability at 5 μm becomes more

significant with increasing fracture length which aligns with the proportion increase at 5 µm illustrated in the figure.

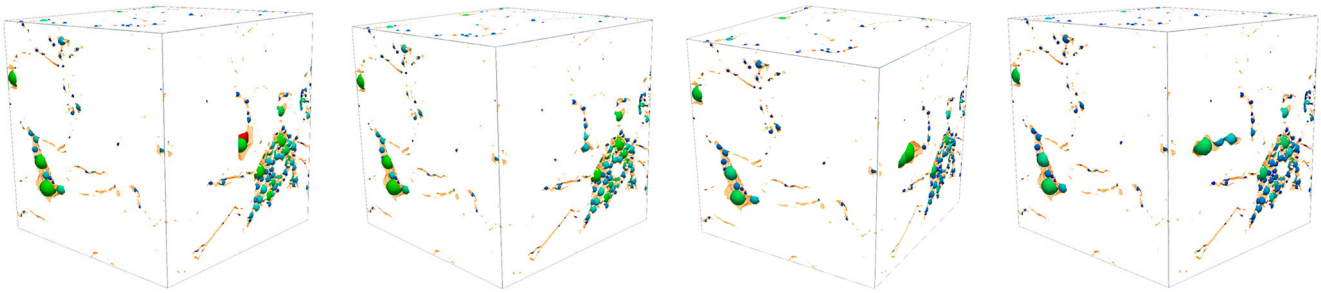

(**a**) length = 50 µm (**b**) length = 200 µm (**c**) length= 300 µm (**d**) length = 450 µm

Figure 9. The digital rocks embedding an artificial fracture with a different length and pore networks extracted using the maximal balls method. (**a**) shows the digital rock and pore network with the micro-fracture whose length is 50 µm, (**b**) is the digital rock and pore network with the micro-fracture whose length is 200 µm, (**c**) represents the digital rock and pore network with the micro-fracture whose length is 300 µm, and (**d**) displays the digital rock and pore network with the micro-fracture whose length is 50 µm.

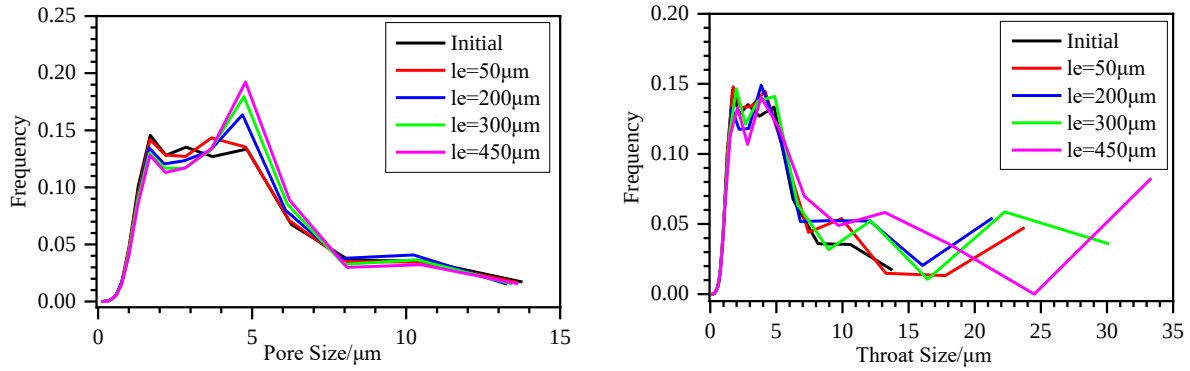

(**a**) Pore radius distribution (**b**) Throat radius distribution

Figure 10. The pore structure distribution of the embedding artificial fracture with different lengths. (**a**) is the pore radius distribution, and (**b**) is the throat radius distribution.

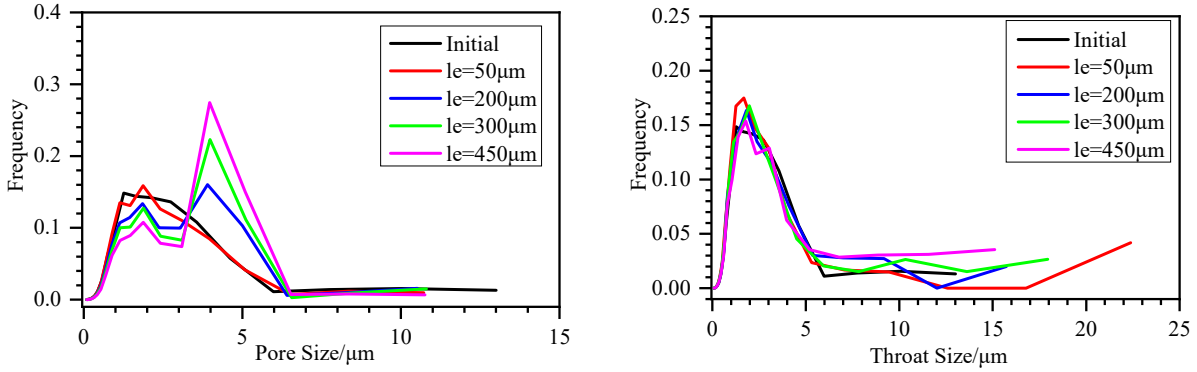

(**a**) The contribution for permeability of the pore (**b**) The contribution for permeability of the throat

Figure 11. The contribution for permeability of embedding an artificial fracture with different lengths. The pore's contribution to permeability is (**a**), while the throat's contribution to permeability is (**b**).

The effect of micro-fracture length on the permeability of a tight sandstone reservoir in different directions was summarized in Table 2. The time needed for each pore network

model is 0.1 h. Table 2 demonstrates that increasing the length of micro-fractures within the rock can lead to increased porosity. Increasing the length of micro-fractures within the rock can lead to increased permeability. Analyzing the permeability in different directions can provide valuable insights into how micro-fractures affect fluid flow.

Table 2. The porosity and permeability of the embedding an artificial fracture with different length.

Different Aperture	Porosity/%	Permeability/10^{-3} μm^2		
		X Direction	Y Direction	Z Direction
Initial	3.21	0.17	0.01	0.10
Le = 50 μm	4.60	0.56	1.46	0.57
Le = 200 μm	5.89	3.77	14.63	1.77
Le = 300 μm	7.66	5.65	572.53	2.82
Le = 450 μm	10.70	298.63	1136.91	2.92

In this study, we investigate the effect of micro-fracture aperture on the permeability of a tight sandstone reservoir in different directions. Our results in Table 2 demonstrate that increasing the aperture of micro-fractures within the rock can lead to increased permeability. This is because micro-fractures significantly enhance the connectivity between pores which allows fluids to flow more freely, as illustrated in Figure 9. Additionally, as the fractures widen, the volume of open space within the digital rock increases, contributing to an overall increase in porosity. However, the relationship between porosity and micro-fracture length is close to linear. Analyzing the permeability in different directions can provide valuable insights into how micro-fractures affect fluid flow. Table 2 shows that as micro-fracture length increases, permeability significantly increases in the X and Y directions. The permeability in the Z direction also increases but much less than in the X and Y directions. As a general trend, micro-fractures that are parallel to the flow direction significantly increase permeability in that direction. This is because micro-fractures provide a clear and unobstructed pathway for fluid flow. However, when a micro-fracture is perpendicular to the flow direction, the increase in permeability may not be as noticeable. This is because micro-fractures do not provide a direct pathway for fluid flow in that direction.

To investigate the impact of micro-fractures length on fluid flow, capillary pressure curves were analyzed in different directions, as shown in Figure 12. The data revealed that, compared to the original model, the capillary pressure curves shifted to the left in the X and Y directions as the micro-fracture length increased. Moreover, significant changes in the capillary pressure curves were observed in these directions when the micro-fracture length, 200 μm. However, the capillary pressure curves in the Z direction showed minimal changes, possibly due to the presence of micro-fractures that run parallel to the XY plane. The relationship between the curves and the direction of fluid flow can be established by comparing the capillary pressure curves in different directions. It is crucial to consider the orientation of micro-fractures when indirectly analyzing the pore structure of cores containing such micro-fractures through capillary pressure curves.

3.3. Embedding an Artificial Micro-Fracture with Different Dip Angle

The direction of fluid flow in tight sandstone reservoirs with micro-fracture can significantly impact their permeability. To investigate this, we added a single micro-fracture to a digital rock of tight sandstone reservoir with an aperture of 10 voxels, a length of 500 voxels, and a dip angle ranging from 0 to 40 degrees. This produced a multi-scale digital rock of the tight sandstone reservoir which is illustrated in Figure 13. The pore network model of the multi-scale digital rock was extracted using the maximal balls method with 0.6 h, as shown in Figure 13.

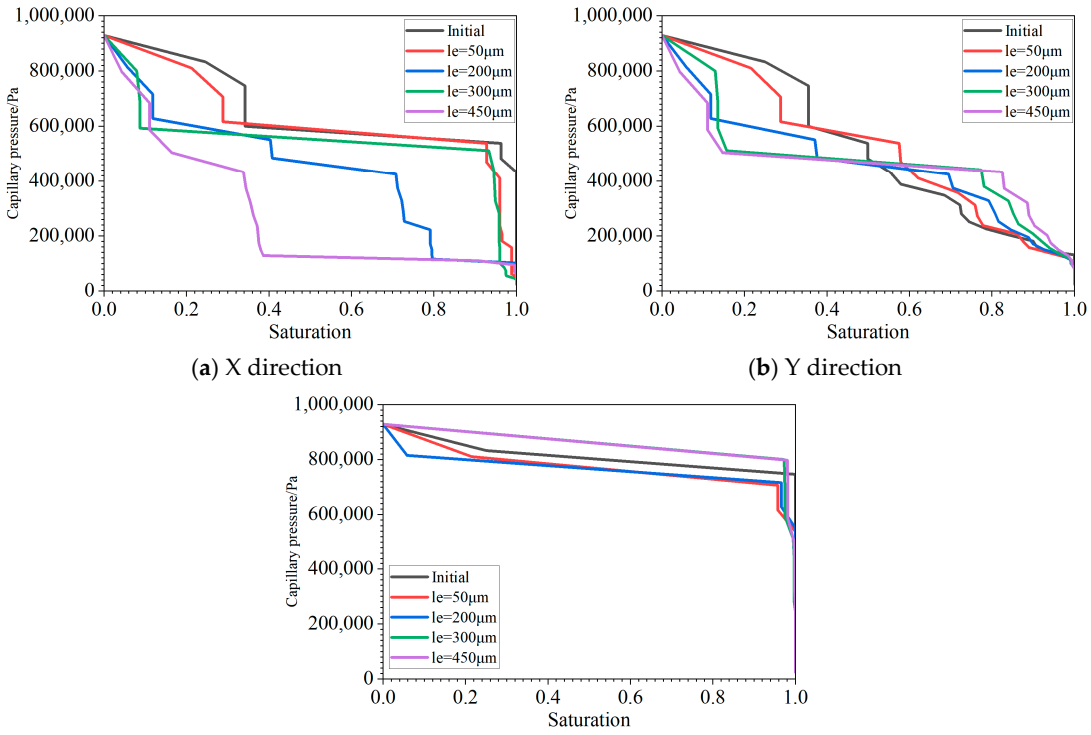

(**a**) X direction (**b**) Y direction

(**c**) Z direction

Figure 12. The capillary pressure curve of the embedding is an artificial fracture with different lengths in different directions. (**a**) is for X direction, (**b**) is for Y direction, (**c**) is for Z direction.

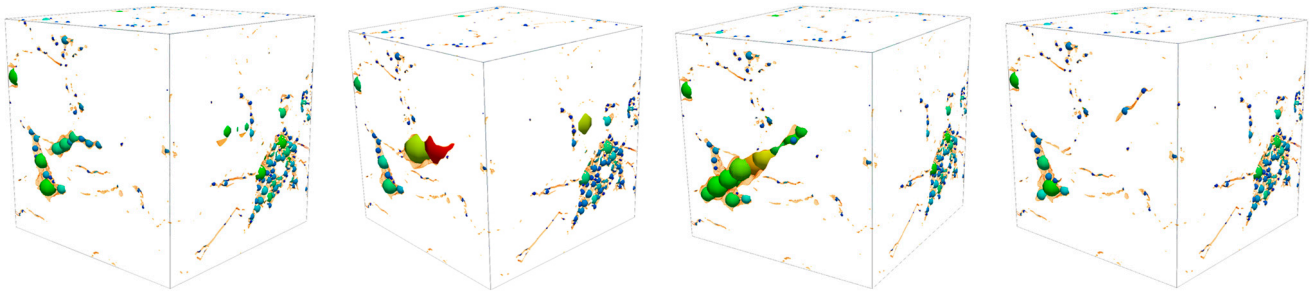

(**a**) angle = 10° (**b**) angle = 20° (**c**) angle = 30° (**d**) angle = 40°

Figure 13. The digital rocks embedding an artificial fracture with a different dip angle and pore networks extracted using the maximal balls method. (**a**) shows the digital rock and pore network with the micro-fracture whose dip angle is 10°, (**b**) is the digital rock and pore network with the micro-fracture whose dip angle is 20°, (**c**) represents the digital rock and pore network with the micro-fracture whose dip angle is 30°, and (**d**) displays the digital rock and pore network with the micro-fracture whose dip angle is 40°.

The impact of the fracture dip angle on the pore throat structure can be observed in Figure 14. The figure clearly indicates that as the fracture dip angle increases, the pore radius distribution remains relatively stable. In contrast, the distribution of throat radius changes from a simple, single-peaked Gaussian distribution to a more complex, double-peaked, or multi-peaked distribution. By examining the values of pore structure contribution to permeability, as depicted in Figure 15, it can be concluded that the intervals with higher contributions to permeability for pore and throat radius are not significantly different from the original core intervals. However, there are more noticeable changes in the intervals with higher contributions to permeability for throat radius.

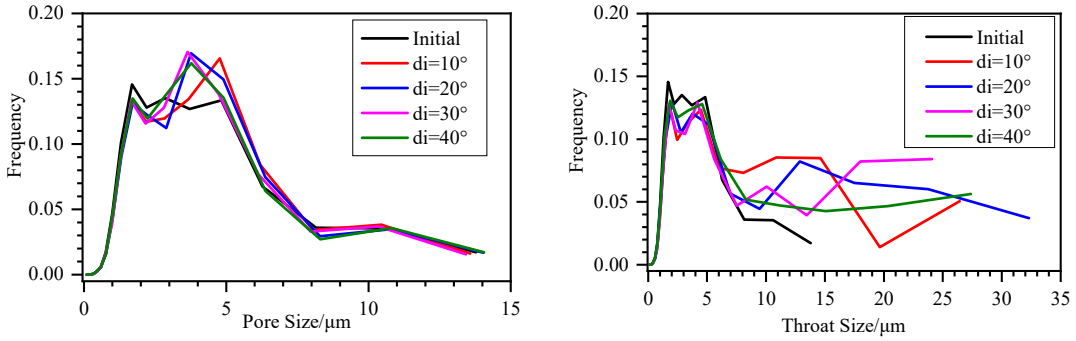

(**a**) Pore radius distribution (**b**) Throat radius distribution

Figure 14. The pore structure distribution of the embedding an artificial fracture with different dip angles. (**a**) pore radius distribution and (**b**) throat radius distribution.

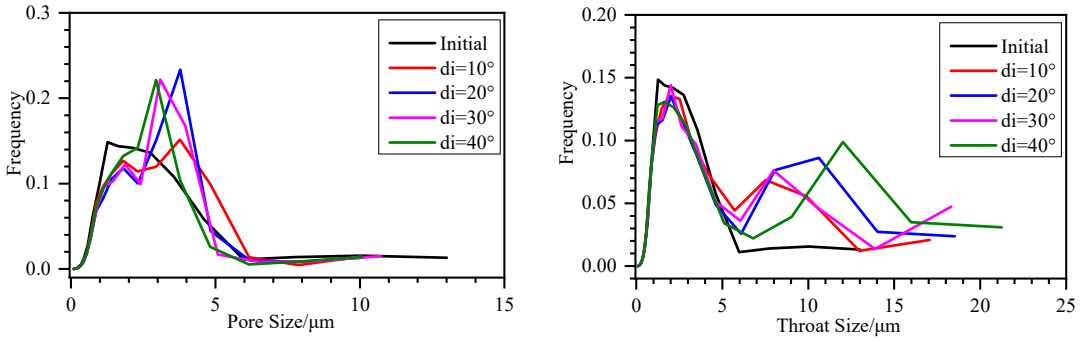

(**a**) The contribution for permeability of pore (**b**) The contribution for permeability of throat

Figure 15. The contribution for permeability of embedding an artificial fracture with different dip angles. The pore's contribution to permeability is (**a**) while the throat's contribution to permeability is (**b**).

Table 3 summarizes the effects of micro-fracture dip angle on the permeability of a tight sandstone reservoir in different directions. The time needed for each pore network model is 0.1 h. As the dip angle of the micro-fracture increases, the permeability in both the X and Y directions initially increases before eventually decreasing. This results from the fact that when the micro-dip fracture's angle grows so does the dip angle between it and the flow directions along the X and Y axes which impacts the permeability in those directions. The permeability in the Z direction remains constant regardless of the dip angle of the micro-fracture.

Table 3. The porosity and permeability of the embedding an artificial fracture with different dip angle.

Different Aperture	Porosity/%	Permeability/10^{-3} μm^2		
		X Direction	Y Direction	Z Direction
Initial	3.21	0.17	0.01	0.10
di = 10°	9.12	220.52	222.43	0.09
di = 20°	9.13	106.85	107.99	0.09
di = 30°	10.37	92.55	93.86	0.10
di = 40°	10.06	0.66	1.32	0.11

The impact of micro-fracture dip angle on fluid flow was investigated by analyzing capillary pressure curves in various directions, as depicted in Figure 16. The figure indicated that, with increasing micro-fracture dip angle, the capillary pressure curves shifted to the

left in the X and Y directions compared to the original model. As the micro-fracture angle decreases, the disparity of the capillary pressure curve between the micro-fracture digital rock and the initial digital rock increases. However, minimal changes were observed in the Z direction. One can determine the relationship between the nature of the curves and the direction of fluid flow by comparing capillary pressure curves in various directions.

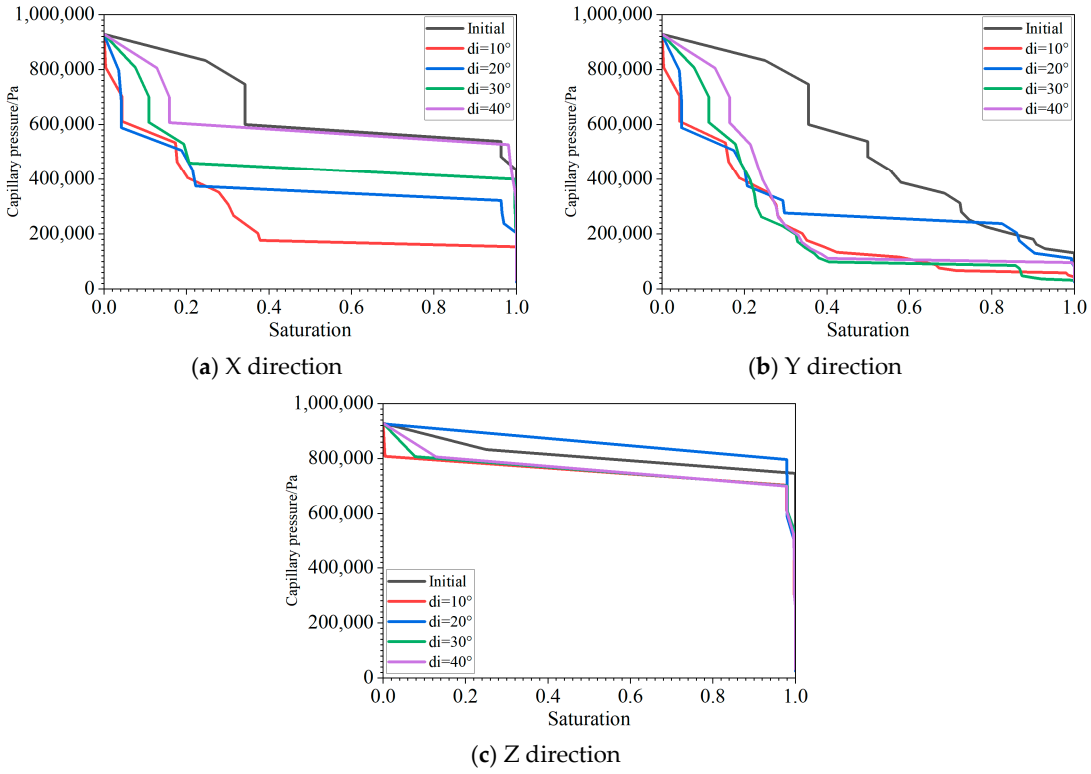

(**a**) X direction (**b**) Y direction

(**c**) Z direction

Figure 16. The capillary pressure curve of embedding an artificial fracture with different dip angles in different directions. (**a**) is for the X direction, (**b**) is for the Y direction, and (**c**) is for the Z direction.

4. Conclusions

This paper utilizes the digital rock analysis technique to investigate tight sandstone reservoirs' pore structure and flow behavior, explicitly considering the impact of micro-fracture characteristics. The study investigated how petrophysical properties are affected by micro-fracture characteristics, such as aperture, length, and dip angle. The findings can be summarized as follows.

1. The application of digital rock analysis technology to tight sandstone reservoirs not only addresses the limitations of traditional experiments for analyzing complex tight sandstone rock samples but also offers the advantages of reproducibility and non-destructiveness. This technique provides insights into the microstructure and flow pattern of the tight sandstone reservoirs which are crucial for understanding their fluid flow behavior. Digital rock analysis technology offers a valuable tool for understanding the complex microstructures of tight sandstone reservoirs and providing critical insights into their properties and behavior.
2. With an increase in both fracture aperture and length, the distribution of the pore throat radius in tight sandstone reservoirs shifts from a conventional Gaussian shape to a bimodal feature, displaying multiple peaks. Furthermore, the contribution of pore throat radius to the permeability of the reservoir remains constant with the increase in fracture aperture and length, emphasizing the crucial role of these two

parameters in determining the permeability. The permeability and capillary pressure curves are significantly influenced by the fracture aperture and length in the direction of connectivity but demonstrate a negligible relationship with these parameters in the non-connective direction.

3. The study has revealed that the dip angle of micro-fractures has a more pronounced effect on the pore throat structure of tight sandstone reservoirs, particularly on the radius of the throat as opposed to the radius of the pore. The permeability and fluid flow within the reservoir are impacted in varying ways by the dip angle of the micro-fracture, with the permeability initially increasing and then decreasing in the X and Y directions as the dip angle increases. This is due to the increased dip angle between the micro-fracture and the direction of fluid flow along these axes. The influence of the micro-fracture dip angle on fluid flow is further demonstrated by shifts observed in the capillary pressure curves, particularly in the X and Y directions. The results suggest a correlation between the direction of fluid flow and the characteristics of the capillary pressure curves.
4. According to the study, an increase in both the aperture and length of micro-fractures leads to an increase in the porosity of the tight sandstone reservoir. However, the effect of the dip angle of micro-fractures on porosity remains uncertain. These micro-fractures are found to improve the porosity and increase the interconnectivity of pores within the reservoir.

Author Contributions: L.L., H.S. and J.Y. conceived the project; L.L. coded the related software and carried out the simulation and analyses and wrote the original manuscript; H.S. and L.Z. provided technical advice throughout the project; K.Z. assisted with the writing of this paper; J.Y. supervised the overall project, and all author contributed to revising and improving the manuscript. All authors have read and agreed to the published version of the manuscript.

Funding: The author thanks the sponsors of this research: the National Natural Science Foundation of China (No. 52034010, 52122402, 12172334, 42090024), Shandong Provincial Natural Science Foundation (No. ZR2022JQ23), the Fundamental Research Funds for the Central Universities (No. 22CX01001A-4), and Program for Changjiang Scholars and Innovative Research Team in University (IRT_16R69).

Institutional Review Board Statement: Not applicable.

Informed Consent Statement: Not applicable.

Data Availability Statement: Not applicable.

Conflicts of Interest: The authors declare no conflict of interest.

References

1. Zeng, L.; Su, H.; Tang, X.; Peng, Y.; Gong, L. Fractured tight sandstone oil and gas reservoirs: A new play type in the Dongpu depression, Bohai Bay Basin, China. *AAPG Bull.* **2013**, *97*, 363–377. [CrossRef]
2. Guo, T.; Tang, S.; Liu, S.; Liu, X.; Xu, J.; Qi, N.; Rui, Z. Physical Simulation of Hydraulic Fracturing of Large-Sized Tight Sandstone Outcrops. *SPE J.* **2021**, *26*, 372–393. [CrossRef]
3. Zhou, J.; Qiao, X.; Wang, R.; Yin, X.; Cao, J.; Cao, B.; Lei, Y.; Tian, K.; Zhao, Z.; Zhugeng, B. Effective reservoir development model of tight sandstone gas in Shanxi Formation of Yan'an Gas Field, Ordos Basin, China. *J. Nat. Gas Geosci.* **2022**, *7*, 73–84. [CrossRef]
4. Gao, H.; Li, H.A. Pore structure characterization, permeability evaluation and enhanced gas recovery techniques of tight gas sandstones. *J. Nat. Gas Sci. Eng.* **2016**, *28*, 536–547. [CrossRef]
5. Lai, J.; Wang, G.; Wang, Z.; Chen, J.; Pang, X.; Wang, S.; Zhou, Z.; He, Z.; Qin, Z.; Fan, X. A review on pore structure characterization in tight sandstones. *Earth-Sci. Rev.* **2018**, *177*, 436–457. [CrossRef]
6. Zhao, S.; Fu, Q.; Ma, W. Pore-Throat Size Distribution and Classification of the Paleogene Tight Sandstone in Lishui Sag, East China Sea Shelf Basin, China. *Energy Fuels* **2020**, *35*, 290–305. [CrossRef]
7. Zhang, J.; Li, Y.; Pan, Y.; Wang, X.; Yan, M.; Shi, X.; Zhou, X.; Li, H. Experiments and analysis on the influence of multiple closed cemented natural fractures on hydraulic fracture propagation in a tight sandstone reservoir. *Eng. Geol.* **2020**, *281*, 105981. [CrossRef]
8. Tan, P.; Jin, Y.; Yuan, L.; Xiong, Z.Y.; Hou, B.; Chen, M.; Wan, L.M. Understanding hydraulic fracture propagation behavior in tight sandstone–coal interbedded formations: An experimental investigation. *Pet. Sci.* **2019**, *16*, 148–160. [CrossRef]

9. Moghaddam, R.N.; Jamiolahmady, M. Fluid transport in shale gas reservoirs: Simultaneous effects of stress and slippage on matrix permeability. *Int. J. Coal Geol.* **2016**, *163*, 87–99. [CrossRef]
10. Lai, J.; Wang, G.; Cao, J.; Xiao, C.; Wang, S.; Pang, X.; Dai, Q.; He, Z.; Fan, X.; Yang, L.; et al. Investigation of pore structure and petrophysical property in tight sandstones. *Mar. Pet. Geol.* **2018**, *91*, 179–189. [CrossRef]
11. Zheng, J.; Zheng, L.; Liu, H.H.; Ju, Y. Relationships between permeability, porosity and effective stress for low-permeability sedimentary rock. *Int. J. Rock Mech. Min. Sci.* **2015**, *78*, 304–318. [CrossRef]
12. Zhang, Z.; Nemcik, J.; Qiao, Q.; Geng, X. A Model for Water Flow through Rock Fractures Based on Friction Factor. *Rock Mech. Rock Eng.* **2014**, *48*, 559–571. [CrossRef]
13. Herz-Thyhsen, R.J.; Kaszuba, J.P.; Dewey, J.C. Dissolution of minerals and precipitation of an aluminosilicate phase during experimentally simulated hydraulic fracturing of a mudstone and a tight sandstone in the Powder River Basin, WY. *Energy Fuels* **2019**, *33*, 3947–3956. [CrossRef]
14. Guo, C.; Xu, J.; Wei, M.; Jiang, R. Experimental study and numerical simulation of hydraulic fracturing tight sandstone reservoirs. *Fuel* **2015**, *159*, 334–344. [CrossRef]
15. Hou, P.; Liang, X.; Gao, F.; Dong, J.; He, J.; Xue, Y. Quantitative visualization and characteristics of gas flow in 3D pore-fracture system of tight rock based on Lattice Boltzmann simulation. *J. Nat. Gas Sci. Eng.* **2021**, *89*, 103867. [CrossRef]
16. Sun, H.; Duan, L.; Liu, L.; Fan, W.; Fan, D.; Yao, J.; Zhang, L.; Yang, Y.; Zhao, J. The Influence of Micro-Fractures on the Flow in Tight Oil Reservoirs Based on Pore-Network Models. *Energies* **2019**, *12*, 4104. [CrossRef]
17. Huang, H.; Babadagli, T.; Li, H.; Develi, K.; Zhou, D. A visual experimental study on proppants transport in rough vertical fractures. *Int. J. Rock Mech. Min. Sci.* **2020**, *134*, 104446. [CrossRef]
18. Song, W.; Yao, J.; Zhang, K.; Yang, Y.; Sun, H. Understanding gas transport mechanisms in shale gas reservoir: Pore network modelling approach. *Adv. Geo-Energy Res.* **2022**, *6*, 359–360. [CrossRef]
19. Liao, Q.; Xue, L.; Wang, B.; Lei, G. A new upscaling method for microscopic fluid flow based on digital rocks. *Adv. Geo-Energy Res.* **2022**, *6*, 357–358. [CrossRef]
20. Blunt, M.J.; Bijeljic, B.; Dong, H.; Gharbi, O.; Iglauer, S.; Mostaghimi, P.; Paluszny, A.; Pentland, C. Pore-scale imaging and modelling. *Adv. Water Resour.* **2013**, *51*, 197–216. [CrossRef]
21. Zhang, D.; Li, S.; Li, Y. Pore-scale investigation on the effect of gas-liquid phase separation on reactive flow in a horizontal rough fracture using the lattice Boltzmann method. *Chem. Eng. Sci.* **2021**, *236*, 116483. [CrossRef]
22. Guibert, R.; Nazarova, M.; Horgue, P.; Hamon, G.; Creux, P.; Debenest, G. Computational permeability determination from pore-scale imaging: Sample size, mesh and method sensitivities. *Transp. Porous Media* **2015**, *107*, 641–656. [CrossRef]
23. Meakin, P.; Tartakovsky, A.M. Modeling and simulation of pore-scale multi-phase fluid flow and reactive transport in fractured and porous media. *Rev. Geophys.* **2009**, *47*. [CrossRef]
24. Zhang, W.; Dai, B.; Liu, Z.; Zhou, C. A pore-scale numerical model for non-Darcy fluid flow through rough-walled fractures. *Comput. Geotech.* **2017**, *87*, 139–148. [CrossRef]
25. Golparvar, A.; Zhou, Y.; Wu, K.; Ma, J.; Yu, Z. A comprehensive review of pore scale modeling methodologies for multi-phase flow in porous media. *Adv. Geo-Energy Res.* **2018**, *2*, 418–440. [CrossRef]
26. Frank, F.; Liu, C.; Alpak, F.O.; Berg, S.; Riviere, B. Direct Numerical Simulation of Flow on Pore-Scale Images Using the Phase-Field Method. *SPE J.* **2018**, *23*, 1833–1850. [CrossRef]
27. Tartakovsky, A.M.; Meakin, P. Pore scale modeling of immiscible and miscible fluid flows using smoothed particle hydrodynamics. *Adv. Water Resour.* **2006**, *29*, 1464–1478. [CrossRef]
28. Yang, Y.; Wang, K.; Zhang, L.; Sun, H.; Zhang, K.; Ma, J. Pore-scale simulation of shale oil flow based on pore network model. *Fuel* **2019**, *251*, 683–692. [CrossRef]
29. Liu, M.; Mostaghimi, P. Pore-scale modelling of CO_2 storage in fractured coal. *Int. J. Greenh. Gas Control* **2017**, *66*, 246–253. [CrossRef]
30. Bultreys, T.; De Boever, W.; Cnudde, V. Imaging and image-based fluid transport modeling at the pore scale in geological materials: A practical introduction to the current state-of-the-art. *Earth-Sci. Rev.* **2016**, *155*, 93–128. [CrossRef]
31. Tahmasebi, P.; Kamrava, S. A pore-scale mathematical modeling of fluid-particle interactions: Thermo-hydro-mechanical coupling. *Int. J. Greenh. Gas Control* **2019**, *83*, 245–255. [CrossRef]
32. Xu, K.; Liang, T.; Zhu, P.; Qi, P.; Lu, J.; Huh, C.; Balhoff, M. A 2.5-D glass micromodel for investigation of multi-phase flow in porous media. *Lab Chip* **2017**, *17*, 640–646. [CrossRef] [PubMed]
33. Su, Y.; Zha, M.; Jiang, L.; Ding, X.; Qu, J.; Jin, J.; Iglauer, S. Pore structure and fluid distribution of tight sandstone by the combined use of SEM, MICP and X-ray micro-CT. *J. Pet. Sci. Eng.* **2021**, *208*, 109241. [CrossRef]
34. Ni, H.; Liu, J.; Huang, B.; Pu, H.; Meng, Q.; Wang, Y.; Sha, Z. Quantitative analysis of pore structure and permeability characteristics of sandstone using SEM and CT images. *J. Nat. Gas Sci. Eng.* **2021**, *88*, 103861. [CrossRef]
35. Balcewicz, M.; Siegert, M.; Gurris, M.; Ruf, M.; Krach, D.; Steeb, H.; Saenger, E.H. Digital Rock Physics: A Geological Driven Workflow for the Segmentation of Anisotropic Ruhr Sandstone. *Front. Earth Sci.* **2021**, *9*, 673753. [CrossRef]
36. Da Wang, Y.; Shabaninejad, M.; Armstrong, R.T.; Mostaghimi, P.; Da Wang, Y.; Liu, S.; Zhao, C.; Regenauer-Lieb, K.; Tung, P.K.M. Deep neural networks for improving physical accuracy of 2D and 3D multi-mineral segmentation of rock micro-CT images. *Appl. Soft Comput.* **2021**, *104*, 107185. [CrossRef]

37. Li, B.; Nie, X.; Cai, J.; Zhou, X.; Wang, C.; Han, D. U-Net model for multi-component digital rock modeling of shales based on CT and QEMSCAN images. *J. Pet. Sci. Eng.* **2022**, *216*, 110734. [CrossRef]
38. Shah, S.M.; Gray, F.; Crawshaw, J.P.; Boek, E.S. Micro-computed tomography pore-scale study of flow in porous media: Effect of voxel resolution. *Adv. Water Resour.* **2016**, *95*, 276–287. [CrossRef]
39. Sheppard, A.P.; Sok, R.M.; Averdunk, H. Improved pore network extraction methods. *Int. Symp. Soc. Core Anal.* **2005**, *2125*, 1–11.
40. Dong, H.; Blunt, M.J. Pore-network extraction from micro-computerized-tomography images. *Phys. Rev. E* **2009**, *80*, 036307. [CrossRef]

Disclaimer/Publisher's Note: The statements, opinions and data contained in all publications are solely those of the individual author(s) and contributor(s) and not of MDPI and/or the editor(s). MDPI and/or the editor(s) disclaim responsibility for any injury to people or property resulting from any ideas, methods, instructions or products referred to in the content.